ARTICLE

Molecular mechanism of Mg^{2+}-dependent gating in CorA

Olivier Dalmas[1], Pornthep Sompornpisut[2], Francisco Bezanilla[1] & Eduardo Perozo[1]

CorA is the major transport system responsible for Mg^{2+} uptake in bacteria and can functionally substitute for its homologue Mrs2p in the yeast inner mitochondrial membrane. Although several CorA crystal structures are available, the molecular mechanism of Mg^{2+} uptake remains to be established. Here we use electron paramagnetic resonance spectroscopy, electrophysiology and molecular dynamic simulations to show that CorA is regulated by cytoplasmic Mg^{2+} acting as a ligand and elucidate the basic conformational rearrangements responsible for Mg^{2+}-dependent gating. Mg^{2+} unbinding at the divalent cation sensor triggers a conformational change that leads to the inward motion of the stalk helix, which propagates to the pore-forming transmembrane helix TM1. Helical tilting and rotation in TM1 generates an iris-like motion that increases the diameter of the permeation pathway, triggering ion conduction. This work establishes the molecular basis of a Mg^{2+}-driven negative feedback loop in CorA as the key physiological event controlling Mg^{2+} uptake and homeostasis in prokaryotes.

---

[1] Department of Biochemistry and Molecular Biology, Institute for Biophysical Dynamics, The University of Chicago, 929 E. 57th Street, Chicago, Illinois 60637, USA. [2] Department of Chemistry, Faculty of Science, Chulalongkorn University, Bangkok 10330, Thailand. Correspondence and requests for materials should be addressed to E.P. (email: eperozo@uchicago.edu).

Magnesium (Mg^{2+}) is the most abundant divalent cation in biology[1] and is essential to all living cells as it participates in a myriad of key physiological and biochemical processes from enzymatic activity to genomic stability. In bacteria, Mg^{2+} homeostasis is carried out by three molecularly distinct translocation systems, MgtA/B, MgtE and CorA[2]. CorA belongs to the GMN (Gly-Met-Asn) family and has been proposed to be one of the major Mg^{2+} uptake pathway[3]. Since the discovery of the *CorA* gene[4], the pioneering work of Maguire and colleagues[5–7] using *in vivo* radiotracer measurement have provided the functional and genetic basis for its role in bacteria. The structures of CorA from *Thermotoga maritima* offered the first structural template to understand Mg^{2+} permeation and transport[8–10]. The GMN family is characterized by relatively low-sequence conservation and several reports have suggested conflicting transport mechanisms for *Tm*CorA[11,12]. However, electrophysiological data show that CorA-driven Mg^{2+} translocation involves a channel-like mechanism where the inwardly biased electrochemical gradient serves as the main driving force for Mg^{2+} permeation[13].

So far, the available *Tm*CorA structures have shown the presence of a density commensurate with a divalent cation at the GMN signature sequence and another ion density located in the cytoplasmic end of the pore[14,15]. This leaves a long (~ 30 Å) narrow pathway without apparent coordination sites for permeating ions, providing no obvious insights in regard to the molecular basis of Mg^{2+} selectivity and permeation for *Tm*CorA and other members of the GMN family. Molecular dynamic (MD) simulations and electrostatic calculations have suggested that the present set of divalent-bound crystal structures represents a non-conductive state[16,17]. A recent structure of a distant *Tm*CorA homologue from *Methanocaldococcus jannaschii* has revealed the first structural glimpses into the determinants of Mg^{2+} selectivity. An electron density asymmetrically positioned in the outer mouth of the pore has been interpreted as Mg^{2+} with its first water shell[18]. Interestingly, this new structure points to a putative role for residue Asn314 at the GMN signature sequence in selectivity. A recent *Tm*CorA structure shows a similar density coordinated by the same residue triad, suggesting that Mg^{2+} coordination by the GMN signature sequence is a common motif within the family[14]. Using a combination of electrophysiology and mutagenesis, we have shown that the GMN motif likely participates in the formation of a high-affinity Mg^{2+}-binding site that defines CorA selectivity via a knock-in knockout repulsion mechanism[13].

Indeed, as derived from the present set of structures, such a long and seemingly inhospitable pore (devoid of ions) has been considered as one of the key arguments, suggesting that widespread conformational rearrangements must take place to allow Mg^{2+} permeation[16,17]. However, attempts to stabilize the conductive conformation of CorA by eliminating divalent ions in the crystallization matrix have been unsuccessful, and the quest for a conductive conformation remains ongoing.

Here we have used electrophysiological and spectroscopic approaches to address two fundamental questions regarding CorA-driven Mg^{2+} translocation: (i) the nature and location of the gate that opens the permeation pathway, and (ii) the molecular movements that underlie Mg^{2+}-driven gating. Using a large set of cysteine mutants targeted to the two transmembrane (TM) segments and the entire stalk helix, we show that binding of Mg^{2+} to the intracellular divalent cation sensor triggers channel closing. Comparison of individual electron paramagnetic resonance (EPR) parameters from the complete set of spin-labelled (SL) mutants provided information on probe dynamics, solvent accessibility and intersubunit distances in the conformationally trapped states. These data, combined with existing crystal
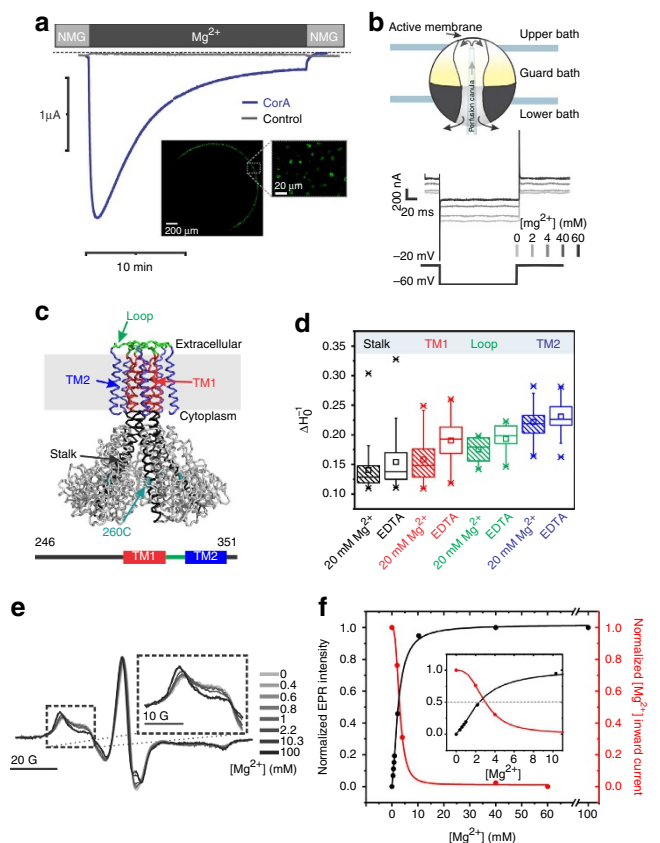

Figure 1 | CorA is gated by intracellular Mg^{2+}. (a) *Tm*CorA-specific Mg^{2+} currents are recorded on a perfused two-electrode voltage clamp setup. The representative traces are recorded at a constant -60 mV for a *Xenopus* oocyte injected with mRNA coding for *Tm*CorA and an oocyte injected with water (control). The currents are recorded with constant external perfusion changing from a divalent-free solution (*N*-methyl glucamine) to a 20 mM Mg^{2+} buffer. The inset represents a confocal microscopy image of an oocyte injected with the YFP-*Tm*CorA fusion construct. (b) The internal perfusion cut-open oocyte voltage clamp setup used for this experiment is schematized in the upper panel. The representative trace is shown in the lower panel for each internal buffer tested. (c) Schematic representation of the cysteine scan used for this work. The covered sequence is shown in black red, green and blue. (d) Statistical representation of the probe mobility parameter ΔH_0^{-1} for the different secondary structure elements. Boxes are the 25–75% with the median as horizontal line, the little squares show the mean values, and the asterisks show the 1–99% using the same colour code as for panel c. (e) CW-EPR spectra recorded for the Q260C-SL mutant in presence of various Mg^{2+} concentrations. (f) Titration plot of the normalized Mg^{2+}-dependent currents superimposed with Mg^{2+} conformational transition recorded by CW-EPR. Both plots were fitted by a Hill equation. The inset is a magnification of the low concentration range.

structures and computational approaches, were used to depict the structural rearrangements associated with Mg^{2+}-dependent gating and to generate three-dimensional (3D) models of CorA in its putative conductive conformation.

Results

CorA is gated by intracellular Mg^{2+}. *In vivo* transport measurements of CorA show that shortly after a rapid Mg^{2+} uptake, its intracellular concentration remains steady, suggesting that the activity of CorA might be self-regulated[19]. Further, *in vitro* studies have revealed a Mg^{2+}-dependent protease susceptibility, a
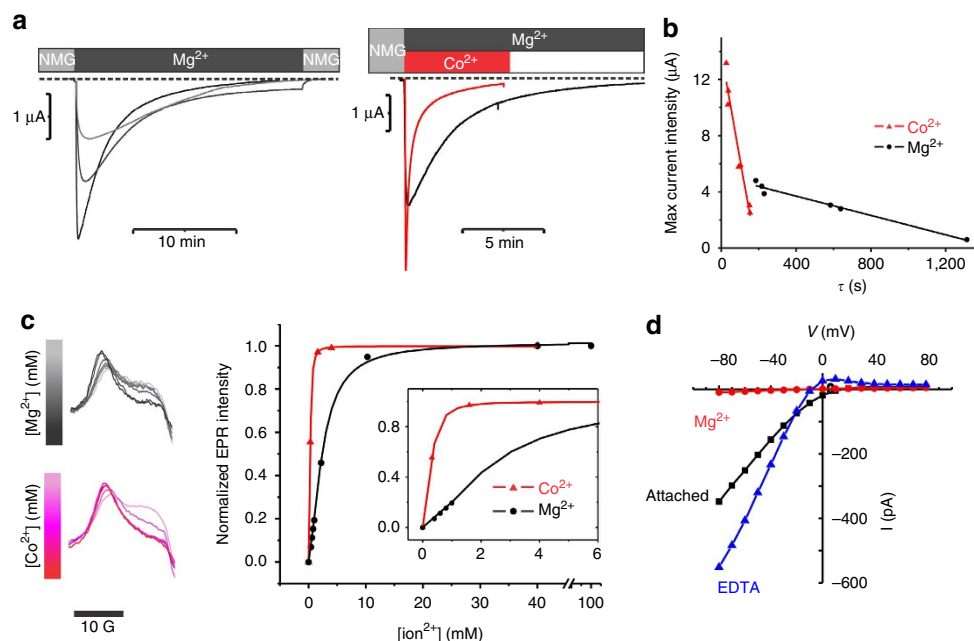
Figure 2 | Divalent cations are both charge carriers and gating factors. (a) Representative traces of Mg^{2+} currents are recorded in CorA-expressing *X. laevis* oocytes clamped at -60 mV. Right trace; Mg^{2+} (20 mM) current traces are in black and the Co^{2+} (20 mM) current is in red. **(b)** Correlation between peak currents and inhibition time constant (single exponential decay fit). The results are plotted in black and red for Mg^{2+} and Co^{2+} as charge carriers, respectively. **(c)** Low-field region of X-band CW-EPR spectra of CorA SL at position 260C titrated by Co^{2+} and Mg^{2+} are shown. The resulting titration plots are displayed using the same colour code for the ions. A magnification of the lower concentration range is displayed in the inset. The plots were fitted with a Hill equation and the apparent affinity is 2.4 mM for Mg^{2+} and 0.29 mM for Co^{2+}. **(d)** I/V curve of excised patch inside in the inside out configuration when the cytoplasmic domain is bathed in presence of divalent chelating compound or a 10-mM concentration of Mg^{2+}.

clear indication that Mg^{2+} translocation through CorA must involve substantial structural rearrangements[10,14,20]. We have generated overexpression constructs that produce large *Tm*CorA-catalysed ionic currents in *Xenopus* oocytes[13]. This Mg^{2+} inward current peaks within a few seconds (a reflection of the speed of the solution exchange) and spontaneously decays over the course of 15–20 min to a small ($<5\%$ of peak) steady-state current (Fig. 1a). The decay time constants are correlated with the current intensity and the nature of the permeant ion, leading us to suggest that internal Mg^{2+} likely serves a dual role as both permeant ion and gating ligand for CorA (Fig. 2). At high intracellular Mg^{2+} concentration (>5 mM), CorA-catalysed currents are small or non-existent but as the intracellular concentration drops below 1–2 mM channel opening is triggered, supporting robust Mg^{2+} inward currents. This was directly confirmed by using a cut-open oocyte setup where the local Mg^{2+} concentration is tightly buffered and constantly perfused through a cannula positioned close to the membrane (Fig. 1b). Under those conditions, the inward current is abolished as a consequence of increasing internal Mg^{2+} concentration with an apparent Mg^{2+} affinity of 2.4 mM, which also corresponds to the physiological concentration in bacteria (2–3 mM)[21]. These conformational transitions are best fitted with the Hill number of 2 ($n_H = 2$) and suggest a positive cooperativity for the Mg^{2+}-driven gating transition (Fig. 1f).

We have investigated the conformation of liposome-reconstituted CorA in the following two different experimental conditions: without Mg^{2+} (apo form) and at saturating Mg^{2+} concentrations (20 mM). Continuous wave EPR spectroscopy (CW-EPR) was used to determine the spectral properties of for more than 100 SL cysteine mutants (Fig. 1c). Figure 1d reports the global change in probe mobility (ΔH_0^{-1})[22] in four different regions of CorA, clearly showing widespread structural rearrangement associated with the presence of Mg^{2+}. From this

large data set, position 260 displays one of the largest spectral changes between the apo and Mg^{2+}-bound forms of CorA, making it an ideal reporter to establish the Mg^{2+} dependence of the conformational changes in CorA (Fig. 1d,e). Assessed from the SL mobility, the overall Mg^{2+} dependence of the structural changes is similar to that obtained for the inhibitory gating measured by perfused cut-open oocyte voltage clamp (Fig. 1f). Equivalent conformational transitions were observed in the absence of a lipid bilayer, implying that the Mg^{2+}-dependent structural changes are self-contained, with no direct participation of the lipid bilayer (Supplementary Fig. 1). We conclude that the Mg^{2+}-driven deactivation of Mg^{2+} currents (Fig. 1a,b) and the Mg^{2+}-induced conformational transitions observed by EPR (Fig. 1e) are a reflection of the very same molecular events that underlie Mg^{2+}-dependent gating in CorA.

This conclusion is further supported by several pieces of information that relate these time-dependent current changes to a fundamental property of CorA gating. First, when Mg^{2+} current are increased by variation of the CorA expression levels, a concomitant acceleration in Mg^{2+} current decay is observed (Fig. 2a,b). Second, other divalent cations such as Co^{2+} are not only able to permeate CorA but also induce current decay with much faster kinetics than those obtained with Mg^{2+} as charge carrier (Fig. 2a,b). Structural rearrangements can be followed as a function of Mg^{2+} or Co^{2+} concentrations and are best fitted by a classical Hill-binding model with an apparent affinity for Mg^{2+} of $K_{0.5} = 2.4$ mM and for Co^{2+} of $K_{0.5} = 0.2$ mM, both showing positive cooperativity ($n_H = 2$) (Fig. 2c). The higher Co^{2+} affinity detected by spectroscopy is consistent with the faster rate of inward current decays (Fig. 2a,b) and with previous Co^{2+}-binding experiments, but is in the toxicity range of this cation that seems incompatible with a role of CorA as a regulator of Co^{2+} homeostasis as previously proposed[11]. Third, excised patch clamp experiments show that exposure of the intracellular domain of
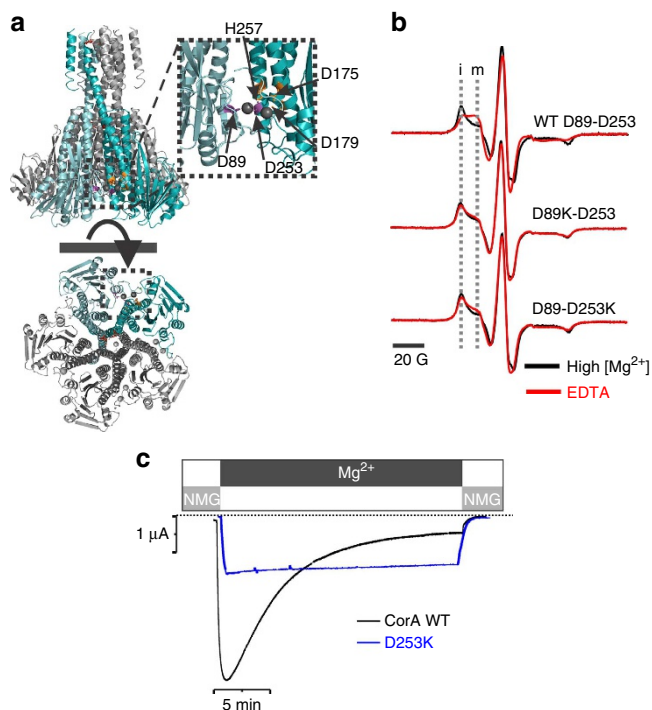
Figure 3 | The divalent cation sensor. (**a**) Close-up view of the putative regulatory Mg^{2+}-binding domain revealed by the crystal structure. (**b**) EPR spectra of the Q260C-SL mutant recorded in presence of 20 mM Mg^{2+} shown in black and in absence of divalent cation shown in red. The experiments were repeated in the background of the WT protein, D89K and D253K mutation. The immobile (i) and mobile (m) components of the low-field spectra are highlighted by two vertical dash lines. (**c**) Representative macroscopic current traces recorded for WT CorA and D253K are shown in black and blue, respectively.

CorA to millimolar concentrations of Mg^{2+} leads to a reduction and, eventually, to the complete inhibition of the CorA-driven Mg^{2+} currents. However, pre-exposing the cytoplasmic side to EDTA under the same experimental conditions consistently enhances Mg^{2+} current amplitudes (Fig. 2d). We interpreted these phenomena to be the result of a self-regulatory mechanism, where an increase in the local Mg^{2+} concentration on the intracellular side of the membrane saturates a CorA Mg^{2+}-binding site, ultimately triggering channel closure. Under this scheme, the apo form of CorA is conductive and Mg^{2+} binding triggers channel deactivation and stabilizes the non-conductive (closed) state of the channel. This mechanism where the charge carrier being also the gating factor fully supports the suggestion that Mg^{2+} homeostasis in bacteria takes place through a Mg^{2+} negative feedback loop[2,10,20].

The divalent cation sensor. The crystal structures of *Tm*CorA obtained in a high concentration of divalent ions (Mg^{2+}, Co^{2+} and Ca^{2+}) point to the likely location of the divalent cation sensor[8,9,10]. A clear electron density was unequivocally assigned to divalent ions coordinated between two aspartate residues, Asp253 from one subunit and Asp89 from its adjacent subunit[8] (Fig. 3a). Mutating these residues alters the Mg^{2+}-dependent protease digestion susceptibility, implying that these residues might be involved in magnesium sensing[10]. Using both spectroscopic and electrophysiological approaches, we find that disrupting the contribution of individual components of this putative site markedly alters Mg^{2+} binding. Replacing Asp253 or Asp89 by a lysine abolishes the Mg^{2+}-dependent conformational

transition observed at position Asn260 (near the divalent-binding site) by EPR spectroscopy (Fig. 3b). Also, given the similarities with the EPR spectra of D89K-D253, D89-D253K and Mg^{2+}-bound wild-type (WT) CorA (again at position Asn260), the conformational equilibrium of the divalent-binding site mutant seems to be biased towards the closed state. This observation is supported by a moderate loss of function phenotype in a cell complementation assay[20]. Based on this observation, we argue that the conformational motions monitored at position 260 directly correlate with the presence of Mg^{2+} at the divalent-binding site. Oocytes injected with the D253K construct can still generate a CorA-specific Mg^{2+} inward current, but in contrast to the WT channel they do not exhibit a time-dependent decay (Fig. 3c), and thus facilitate permeation studies[13]. This result is the most direct demonstration that the interacting pair Asp253-Asp89 acts as an important component of the divalent cation sensor in CorA. This divalent sensor presumably probes the intracellular concentration of Mg^{2+} and triggers an allosteric conformational wave that leads to channel closure as Mg^{2+} reaches above its physiological level. Interestingly, MgtE also seems to operate with a self-regulated mechanism despite any structural nor sequence similarity to CorA[23,24].

Gating involves expansion of the intracellular cavity. To gain further insight into the CorA-gating mechanism, we carried out a complete characterization of the environmental properties of SLs attached to cysteine residues located along the long stalk helix (residues 246–293), the pore-forming TM1 helix (residues 294–314), the extracellular loop (residues 315–325) and the lipid-facing TM2 helix (residues 326–348). We analysed three structural parameters from CW-EPR spectral properties such as probe mobility (ΔH_0^{-1}) that reflects the conformational flexibility[22] (larger ΔH_0^{-1} values imply higher motional freedom); collision with NiEDDA, an indicator of water exposure; and collision with O_2 that monitors lipid exposure[25,26] (Fig. 4a). Measurements were carried out in high Mg^{2+}, which should favour the closed conformation, and in the nominal absence of Mg^{2+} (or other divalent ions), which should populate the open state of CorA.

Comparing solvent accessibility and probe mobility revealed a series of marked Mg^{2+}-driven structural changes in CorA (Fig. 4b). In the Apo form, residues from the stalk helix forming the inner cavity of the intracellular funnel show increased mobility and NiEDDA accessibility ($\Pi NiEDDA$), particularly for residues Gly274, Leu280, Val283 and Thr287. Differences in $\Pi NiEDDA$ between the apo- and Mg^{2+}-bound states mapped onto the crystal structure of *Tm*CorA (closed state; Fig. 4b) show that the major increases in $\Pi NiEDDA$ and ΔH_0^{-1} take place inside the funnel cavity (arrows). These results point to a widening of the inner funnel cavity as Mg^{2+} is removed from its regulatory domain. Consistent with the fairly large cavity expansion, the sharp increase in probe mobility seems to occur in both faces of the helix as a result of reduced helical packing in the open (apo) conformation. Given the size of NiEDDA compared with a water molecule, we anticipate that the functionally relevant magnitudes of the conformational transitions extend further beyond the mapped increases and represent a widespread reorientation of the permeation pathway as a whole. This is supported by significant changes in the O_2 accessibility (ΠO_2) along the TM helices (Fig. 4d). The relatively large increase in ΠO_2 profile along pore-facing residue in TM1 indicates a relative reorientation of this helix (Fig. 4c). These changes are compatible with the unbending of helix TM1, ultimately leading to an increase in the diameter of the permeation pathway. The very high ΠO_2 values reported for TM2 indicate that the intimate
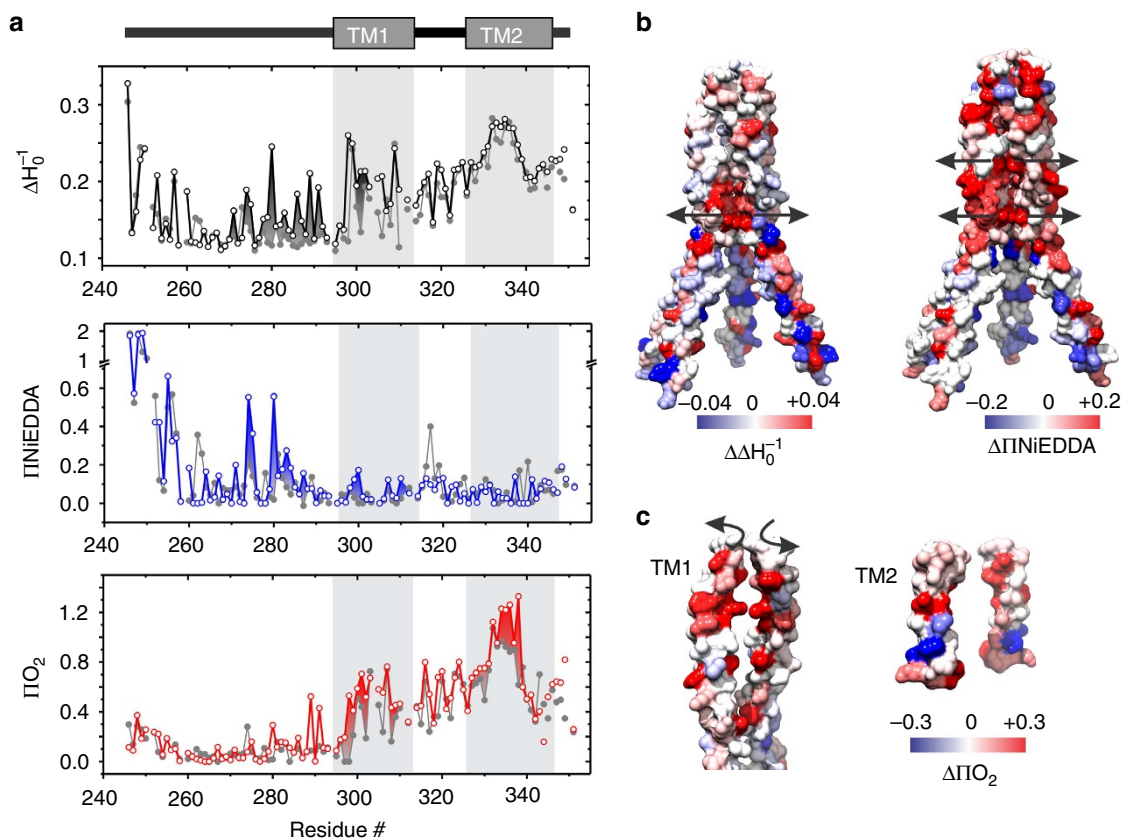
Figure 4 | Probe environmental parameters and structural rearrangement associated with gating. (a) Probe mobility, NiEDDA accessibility and O_2 accessibly values were plotted against the residue number for two experimental conditions: 20 mM Mg^{2+} and no Mg^{2+}. The values for sample recorded in presence of Mg^{2+} (closed state) are shown in grey closed circle, whereas the values obtained for CorA in its open conformation are shown as coloured open circles. **(b)** The differential mobility values between the open and the closed conformation were colour coded from red to blue and mapped on the crystal structure of CorA. For clarity purposes, only the stalk helix and Tm1 are shown and one subunit has been removed. Similar representation is shown on the right side for the differential values in NiEDDA colliding agent. **(c)** Differential O_2 accessibility are colour scaled and mapped on TM1 (left panel) and TM2 (right panel). Only two subunits are shown for clarity purposes.
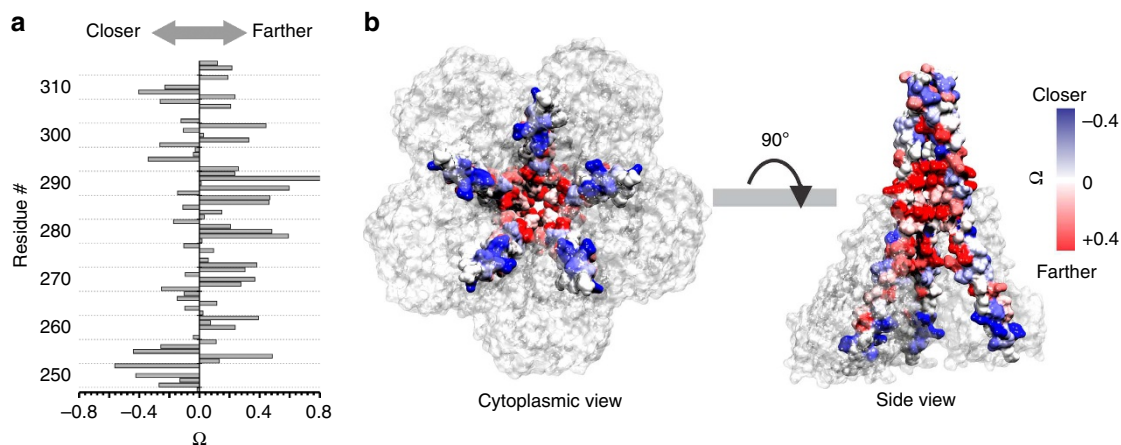

Figure 5 | Change in intersubunit proximities in the Stalk and in the pore-forming TM1 helices. (a) The bars represent the Ω parameter that reports on the relative intersubunit proximity change when the channel goes from the closed to the open state. Ω is defined by the ratio of the intensities of the central resonance line of the EPR spectra for the same sample in presence of 20 mM Mg^{2+} and in absence of Mg^{2+} (see Methods section). **(b)** Ω values are colour scaled and mapped on the CorA crystal structure (closed conformation). Two views are presented and for clarity purposes TM2 has been removed and on the side view one subunit has been removed so the pore-facing residues are visible.

contact between TM1 and TM2 are disrupted in the open conformation. Conformational changes were also observed for TM1 as evaluated from the collision to the DOGS-NTA[Ni(II)] lipid, a collisional agent that reports on interfacial accessibility (Supplementary Fig. 2). This strongly supports a sizable and widespread structural rearrangement upon Mg^{2+}-driven gating

that appears to be larger than the relatively modest radial and lateral tilts of the stalk helix α7 recently reported[14].

Inner motion of the stalk helix leads to pore opening. As expected from a radially symmetric homopentameric protein, line shape analyses of CorA EPR spectra reveal the presence of strong spin–spin interaction at residues facing the five-fold symmetry axis along the pore[17]. Any movement that alters the intersubunit proximity would generate changes in the spin–spin coupling of spatially close residues (≤ 15 Å). Because of the complications owing to the distance relations in a pentameric geometry, we have estimated the intersubunit relative proximity from the ratio of the normalized amplitude of the spectra in the open and closed conformation (the Ω parameter adapted from Perozo et al.[27], see Methods section). Negative Ω values indicate that the labelled positions are moving closer to the five-fold axis of symmetry, whereas positive Ω values reflect motion away from the symmetry axis. Plotting the Ω values versus the residue sequence revealed that residues at the tip of the C-terminal end of the stalk helix move closer to the symmetry axis as the channel opens (Fig. 5a,b). Beyond residue Asp270, the vast majority of the positions move further away from the centre, indicating an expansion of the cavity and permeation path (Fig. 5b). In the closed conformation structure, we and others have shown that permeation of a point charge through CorA is limited by several energy barriers along the permeation pathway[16,17]. Any conformational change triggering CorA opening must lower the amplitude of these barriers. Considering the presence of a kink in the stalk helix at position Gly273 and a pivot point, it is conceivable that a closure of the tip of the stalk helix would translate into an expansion of the funnel and the permeation pathway (Supplementary Fig. 3). Dipolar coupling at positions flanking the constricted permeation pathway clearly indicate the dilation of the permeation pathway throughout its length, supporting the idea of an open channel (Supplementary Fig. 4).

This type of structural rearrangement is incompatible with a classical transporter-like mechanism where the protein alters its conformation from an inward facing to outward facing conformation by means of a rocking motion. This interpretation is also supported by the anomalous mole fraction effect observed in Ni^{2+}/Mg^{2+} mixtures, indicating that CorA pore is multi-occupied[13]. Our results are also consistent with MD simulations data suggesting an iris-like mechanism of opening[16]. To quantify the amplitude of the motion described above, we carried out double electron-electron resonance (DEER) spectroscopy experiments to calculate the average distances and distance distributions of interprobe distances[28] under different Mg^{2+} concentrations. Recently, we have shown that using a symmetry-based constraints fit, we can accurately measure distance distributions on homomeric proteins[29]. Labelling positions at residues Thr247, Pro249, Tyr250 and Arg252 were selected to be within the working distance range of the DEER technique (20–70 Å). Figure 6 shows that for the four positions at the end of the stalk helix, both the short adjacent and the long diagonal distance in the pentamer decrease ~ 5 Å when the open state is populated (Supplementary Table 1). These measurements describe a relatively large closure movement of the stalk helix upon gating (Fig. 6b). The larger amplitude of the distance distribution in the open channel is compatible with an increase of protein dynamics that could interfere with the crystallization of this conductive conformation[14]. Such a movement is likely to dampen away from the hinge point and is expected to produce sufficient torque to propagate into the permeation pathway (TM1), generating the relatively large pore widening suggested above on the basis of the changes in environmental parameters (Fig. 4).
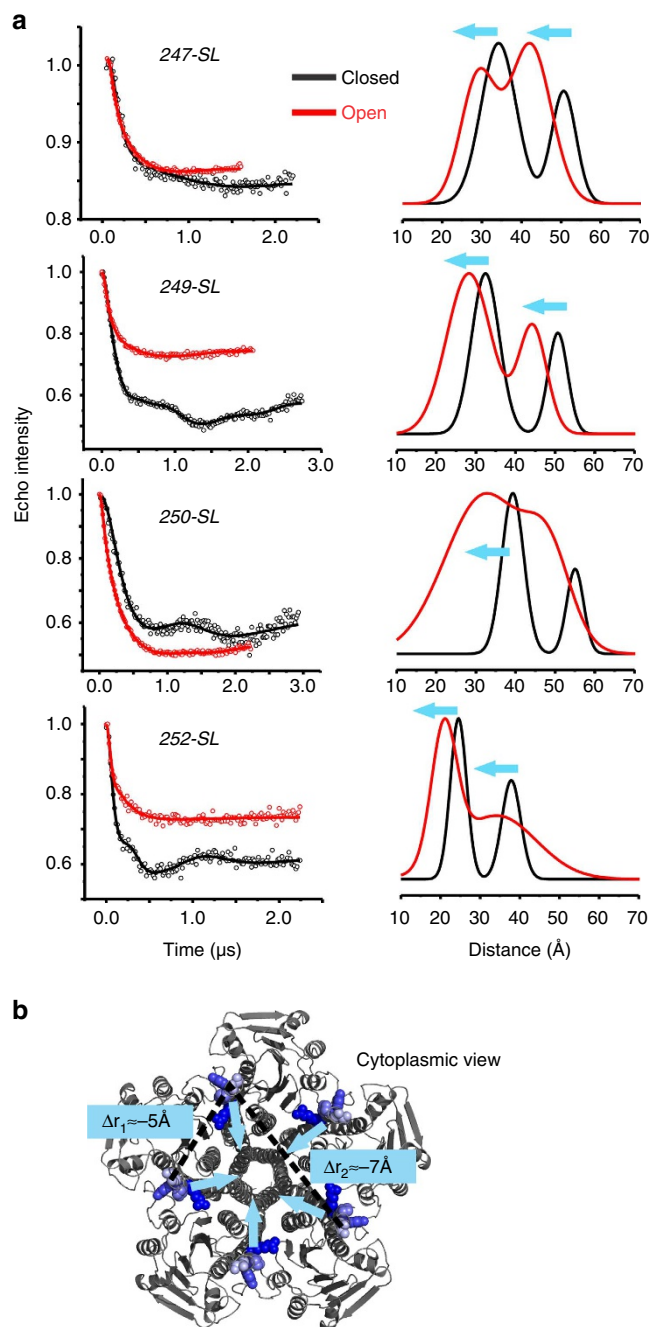

Figure 6 | Quantification of the stalk helix inward motion by DEER spectroscopy. (a) Background-corrected dipolar evolutions are shown as open circles for four different mutants. The fitted data are represented as solid lines and the corresponding distance distributions are illustrated using the same colour code. **(b)** The labelled positions are shown in blue on the cytoplasmic view of CorA crystal structures. Two dotted line represent the adjacent $<r_1>$ and the diagonal $<r_2>$ components of the distance distribution and the blue arrows schematize the inferred motion.

A model of CorA in its open conformation. We have taken advantage of the present set of structural data as constraints to build 3D models of CorA in its open conformation. Accessibility data together with intersubunit distance changes were applied to the existing 'closed' conformation structure (Mg^{2+}-bound) by means of restrained MD simulation using solvent accessibility as a soft constraint[30] (Fig. 7 and Supplementary Figs 6 and 7). Model generation was limited to the regions of CorA from which experimental data is available, including the long stalk
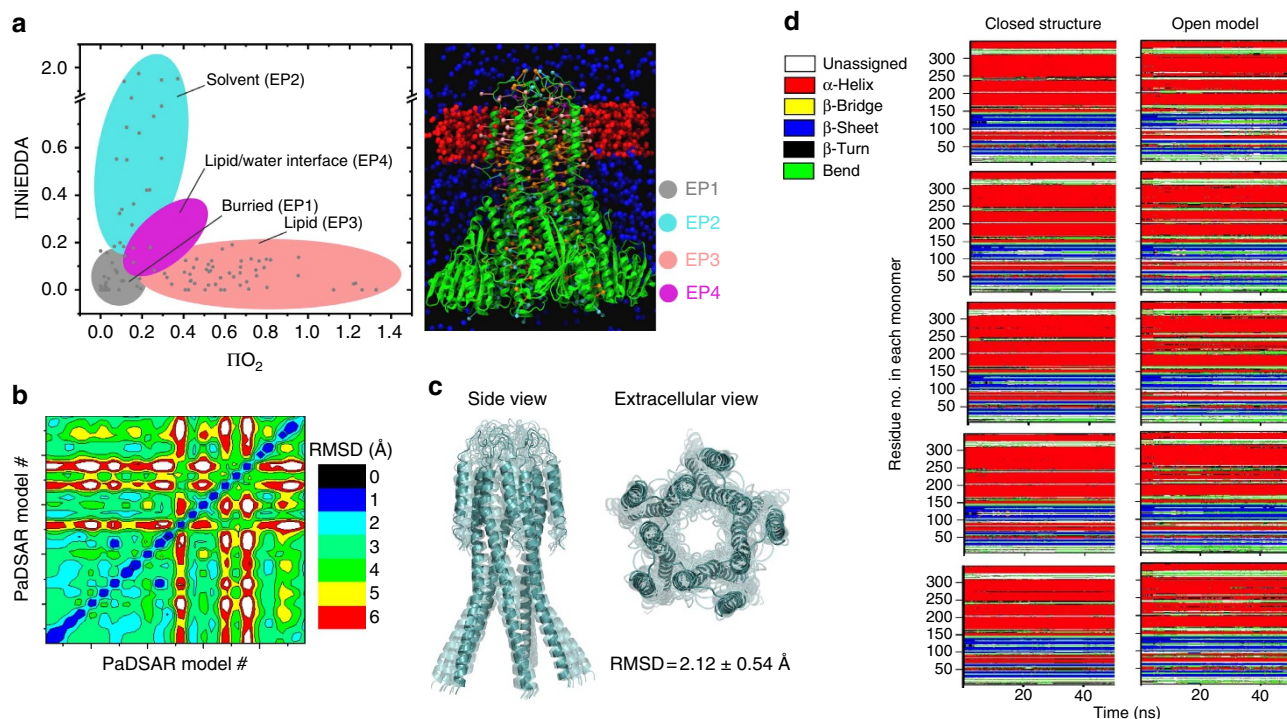
Figure 7 | Structural model building and validation for CorA in its open conformation. (a) PaDSAR translates solvent accessibility into structural restraints[30] (for details see Methods section and Supplementary Fig. 6). The pseudoatom probes are classified in four categories according to their EPR environmental parameters (left panel) and the starting structure (right panel) is equilibrated into a slab of O_2 molecules, representing the lipid bilayer (red spheres). NiEDDA relaxing agent is represented by blue spheres. **(b)** Hundreds of models were generated and evaluated according to their agreement with experimental data (Supplementary Fig. 7). The 25 best models candidates were selected for a second round of PaDSAR refinement and the pairwise Cα-RMSD matrix of the 25 PaDSAR models are colour scaled and coded on the contour plot. **(c)** An ensemble of 10 models show strong converging structures with backbone RMSD of 2.1 Å ± 0.5 for the regions where EPR data were obtained. **(d)** An all-atoms MD simulations of closed and open CorA embedded in a hydrated lipid bilayer was performed. Secondary structure elements were assigned according to DSSP algorithm[52]. Stability of the closed and open structures secondary structure elements was followed during the time course of the unrestrained MD simulation. The residue run from 6 to 349 are coloured coded depending on their secondary structure as followed: α-helix (red), stand in β-sheet (blue), β-bridge (yellow), β-turn (black), coil (green), unassigned (white).

helix, the TM helices and the extracellular loop. The accessibility restraints were enforced through Lennard–Jones-like interactions between a pseudoatom representation of the SL and environmental probe-surrounding particles[30] (Fig. 7a). Intersubunit Cβ–Cβ distances estimated from DEER experiments, together with the accessibility data, were used to generate multiple models by varying the distance constraint boundary, increasing MD refining cycles and replicating the pentamer structure from individual subunits (Supplementary Table 2). After validation, the top 25 models were subsequently refined using the accessibility restraints (Fig. 7b and Supplementary Fig. 7). After a second round of refinement, the top 10 models show good structural convergence with a root mean square difference (RMSD) of 2.12 ± 0.54 Å of each other (Fig. 7c). The stability of the top-ranked structure was evaluated by an all-atom MD simulation in a fully hydrated phospholipid bilayer. After 5 ns of simulation, the stalk and inner helices are stable ~3–5 Å RMSD from the starting structure for the whole-simulated time (25 ns) (Supplementary Fig. 8). From the simulations, few transient changes in secondary structure of the open model are observed but the overall secondary pattern of the open model is similar to that of the closed structure (Fig. 7d). This suggests that the open model is a plausible structure for CorA in its open conformation.

Superimposing the two CorA permeation pathway models offers a glimpse of the nature and extent of the conformational transition taking place during Mg^{2+}-driven gating (Fig. 8). The tips of the stalk helix come together towards the axis of symmetry

like the nozzle of a jet-engine. After a kink, this motion translates into an expansion of the cavity and the mouth of the pore opens up with a motion reminiscent of an iris of a camera. These conformational transitions are best appreciated by observing the linear interpolation between the two states and illustrates the negative feedback mechanism first anticipated by Maguire and colleagues[5–7] (Supplementary movie). Given the low resolution of our spectroscopic approach, we choose to analyse the pore radius profile of our 10 best-ranked models (Fig. 8b). The comparison of the two conformational states clearly indicates a pore expansion throughout the length of the permeation pathway. Interestingly, the expansion is relatively modest on the upper part of the pathway around the signature sequence residues, consistent with their putative participation in Mg^{2+} selectivity[14,18]. The pore dilation is larger ($+5$ Å) for the most constricted region of the pore, especially for the hydrophobic gates formed by Met292 and Leu294. These increases in the pore radius profile are consistent with expectations for an open channel, and suggest that our average model represents a plausible structure for the conductive state of CorA. Poisson–Boltzmann (PB) electrostatic calculation performed on our 10 best-ranked models shows that the large energy barriers impeding ion conduction in the closed state are largely alleviated (Supplementary Fig. 9). Altogether, our results support an explicit molecular mechanism of magnesium regulation in prokaryotes where CorA acts as a Mg^{2+}-deactivated Mg^{2+}-selective channel as part of an homeostatic negative feedback loop (Fig. 8c).
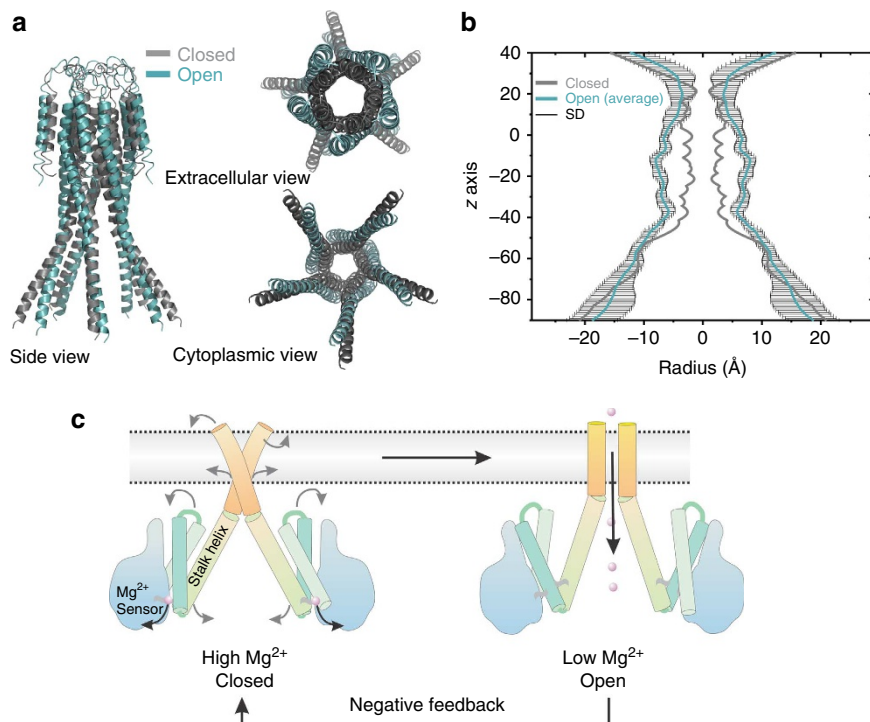
Figure 8 | Mg²⁺-dependent gating mechanism of CorA. (a) The open model generated by restrained MD simulation is shown in teal and the closed-state crystal structure is shown as grey cartoon. Only the positions measured by EPR are shown. **(b)** The pore radius profile was calculated for our 10 best-ranked open models using the program HOLE[40]. The average value is plotted in teal colour and the s.d. values are plotted in black. The profile for the closed structure is plotted in grey colour for comparison. **(c)** Cartoon summarizing the structural rearrangements is associated with the Mg²⁺-gating process regulating closing and opening of CorA. When the intracellular [Mg²⁺] drops below 2 mM, Mg²⁺ leaves its regulatory-binding site, triggering a closing motion of the stalk helix. This motion propagates as a widening of the permeation pathway switching the conformation to a conductive state.

Methods

Molecular biology and *Xenopus laevis* oocyte overexpression. CorA from *T. maritima* was sub-cloned in the pbstA vector optimized for oocyte expression[31] using the unique restriction sites NcoI and Xba1 and the PCR primers 5′-AAAAACCATGGAGGAAAAGAGGCTGTCTGCT-3′ and 5′-AAAAATCTAG ATTAGAGCCACTTCTTTTTCTTGAA-3′. For expression assay only, the same gene was cloned in C-terminal fusion with Venus, a brighter version of the fluorescent protein YFP[32] using the primers 5′-AAAAAACTAGTATGGGCAG CAGCCATCATCATCAT-3′ and 5′-AAAAATCTAGATTAGAGCCACTTCTT TTTCTTGAA-3′ and unique restriction site SpeI and XbaI. Expression was monitored after 24 and 48 h of injection by confocal microscopy on an Olympus DSU Spinning Disk Confocal microscope on oocyte injected with constructs and with blank as control. Mutations were introduced by PCR using mismatch mutagenic primers as described by the Stratagene Quick Change kit. All mutant plasmid were amplified in *Escherichia. coli* XL-1 Blue Strain and purified by Mini or Midi Prep kit (Qiagen) and verified by whole-gene sequencing. Plasmid DNA (10 μg) were linearized by overnight Not1 digestion, verified by 1% agarose electrophoresis and purified by the QIAquick PCR purification (Qiagen) following the suppliers recommendation. Purified linear DNA (1 μg) was used as template for *in vitro* transcription (Ambion) and after purification the RNA were aliquoted and kept frozen at −80 °C. Oocyte were harvested from survival surgery on adult frog according to standard protocol and injected with 50 ng of mRNA.

Electrophysiology. Electrophysiology measurements were performed on custom-made two-electrode voltage clamp setups according to basic standards procedure[33]. The external solutions were isosmotic and typically composed by Hepes/*N*-methyl-D-gluconamide (NMG) 10 mM, NMG-methanesulfonic acid, 30 mM NMG-Cl and 20 mM MgCl₂. The cut-open oocyte preparation was used in experiments requiring control of intracellular [Mg²⁺]. This consisted of a Vaseline-gap oocyte chamber following the original design of Perozo *et al.*[34], where an internal perfusion cannula runs through the internal and guard compartments using a small stainless steel needle (33 gauge) connected to a syringe pump. After mounting the oocyte in the chamber, a micro needle was inserted midway through the bottom of the oocyte and perfusion was begun with internal solution buffered with a mixture of EDTA/ EGTA. Internal Mg²⁺ was successively increased from 0 to 2, 4, 40 and 60 mM by changing the internal perfusion solution. The internal perfusion rate was constant

at 10 μl h⁻¹, and 10–15 min was required for equilibration at each new internal [Mg²⁺].

Sample preparation and CW-EPR spectroscopy. Cysteine mutants were expressed in *E. coli* BL21DE3-pLysS strain as previously described[17]. Immediately after elution from the Co²⁺ column, the purified protein were reacted with a 10 molar excess of SL for 30 min on ice, followed by second addition of 10 molar probe excess and reacted for an additional 30 min. The reaction was stopped by addition of 1,000-fold excess of L-cysteine and the excess probe was removed by gel filtration chromatography. Reconstitution was carried out by destabilizing the pre-formed 1-palmitoyl-2-oleoyl-sn-glycerol-3-phosphatidylcholine (POPC)–POPG 3:1 liposomes with a saturating concentration of Triton X-100 (0.2 (w/w) ratio) before adding labelled protein to the liposome suspension in a 1/1500 protein/lipid molar ratio. Detergent was removed by successive addition of Bio-Beads SM-2 (Bio-Rad) and proteoliposomes were harvested by ultracentrifugation at 200,000*g* and resuspended into 200 μl. Samples were split into two and were equilibrated with a buffer containing either 1 mM EDTA or 20 mM MgCl₂. CW-EPR spectroscopic measurements were performed at room temperature on a Bruker EMX X-band spectrometer equipped with a dielectric resonator (ER 4123D). SL samples were loaded into a gas-permeable TPX plastic capillary and spectra were recorded at 2.0 mW incident power, 100 kHz modulation frequency with 1.0 G of modulation amplitude. The motional freedom of the SL was quantified as a peak-to-peak first-derivative width of the central resonance line (ΔH_0^{-1})[22]. Solvent exposure was measured form power-saturation experiments in which the vertical peak-to-peak amplitude of the central line of the EPR spectra is measured as a function of increasing incident microwave power[25,26]. Prior and during the recording of the spectra the sample are equilibrated with N₂, air (20% O₂) or with 25 mM NiEDDA (Ni[II]ethylenediaminediacetic acid) in presence of N₂. Accessibility parameters Π were calculated as described in a previous report[17]. High accessibility of the spin probe to O₂ is witnessed by a high value of the Π_{O_2} and is diagnostic of a membrane exposed residue, whereas high NiEDDA accessibility (Π_{NiEDDA}) is diagnostic of a water-exposed residue. The relative probe proximity change was determined by calculating the Ω parameter. The Ω parameter is defined by the ratio of the intensities of the central resonance line $M = 0$ for the same sample exposed in two different experimental conditions as followed: $\Omega = \overline{A^{\circ}}/\overline{A} - 1$ where $\overline{A^{\circ}}$ is the amplitude of $M = 0$ measured in absence of Mg²⁺ (open conformation) and $\overline{A}$ is the amplitude of

$M = 0$ measured in presence of 20 mM Mg^{2+} (closed conformation). We shifted the axis with the operator -1 to scale the values for negative/positive values instead of below/above 1.

DEER experiments. Samples concentration was empirically optimized to 75 μM of CorA pentamer and were loaded into a quartz capillary (Vitrocom) and equilibrated at 80 K under a flow of liquid N_2 using an Oxford cryostat. A standard four-pulse DEER sequence was conducted on a Bruker Elexsys 580 EPR spectrometer equipped with a 3-mm split-ring resonator. The four-pulse DEER sequence was set with pulses of 16 ns (90°) and 32 ns (180°), and evolution times were typically set to 1,800–2,500 ns depending on distance and signal quality. Refocused echo intensity evolutions were recorded, and these phase-corrected signals were background-corrected assuming a homogeneous 3D distribution (Supplementary Fig. 5). The distance distribution P(r) was recovered from DEER measurements by a model fit of a two-component $Rice_{3D}$ mixture with distance ratio constraint using $1.578 < k < 1.645$ as determined from our previous study[29]. Analysis was performed on a modified version of DeerAnalysis 2011 programme[35]. Each time domain dipolar evolution data set was preprocessed using tools provided by DeerAnalysis to correct for experimental phase errors and to separate the intramolecular distances from the intermolecular background contribution. The background was assumed as a homogeneous distribution in three dimensions, appropriate for SL membrane proteins in detergent micelles.

Molecular modelling. The starting structure of CorA was taken from our previous work[17]. As mentioned previously, this model of the closed state of CorA was derived from the crystal structure (PDB 2UIB) with remodelling of the unresolved loop (residues 315–325). The structure of CorA is a homopentamer with 344 amino-acid residues per monomer starting from residues 6 to 349. For the calculation of the CorA open model, we used our previously developed method called PaDSAR (pseudoatom driven solvent accessibility refinement), restrained MDs using EPR accessibility restraints[30]. For the present work, the PaDSAR method has been incorporated in CHARMM c35b6 (ref. 36). Two sources of experimentally based restraints used in PaDSAR are the interprobe distances and solvent accessibility data. The detailed method is described below. Analyses of intersubunit DEER distances and the proximity profile of the open and closed states of CorA allow one to estimate a range of distance changes of the labelled positions at the backbone level. In the structure calculation, distance restraints ($\Delta r C\beta$) were defined as a distance difference between intersubunit $C\beta$-positions of the labelled residues measured between the candidate open model and the closed-state X-ray structure as follow:

$$\Delta r_{C\beta,i} = r_{C\beta,i,open} - r_{C\beta,i,closed} \qquad (1)$$

where i is the residue number, of which the experimentally derived distance accounted for the following residue pairs: 247–247′, 249–249′, 250–250′ and 252–252′ (the prime is used to denote different subunits). As a pentameric protein, the 'short' and 'long' distance restraints were used to keep five subunits arranged about a five-fold symmetry axis. The short distance defined an intersubunit $C\beta$–$C\beta$ separation of the residue between a subunit and its first adjacent subunit. whereas the long distance defined that of the residue between a subunit and its second adjacent subunit. From experimental data, the short and long distance restraints were set to $-5 \pm \delta$ Å and $-7 \pm \delta$ Å, respectively. The negative value of distance indicates that the residue pair of an expected open model is getting closer with respect to that of the closed-state structure. The δ values were used to define the upper and lower bound. A list of the intersubunit $C\beta$–$C\beta$ distance restraints used in the calculations is given in Supplementary Table 2. The accessibility restraints used in PaDSAR were derived from the experimental ΠO_2 and $\Pi NiEDDA$ accessibility data of more than 100 SL CorA mutants. The SL-positions covered a broad region of the protein domain including the long stalk helix (residues 246–293), the pore-forming TM1 helix (residues 294–314), the extracellular loop (residues 315–325) and the lipid-facing TM2 helix (residues 326–348). The restraints are described in terms of the Lennard–Jones-like interactions between various types of spin probe pseudoatoms attached to the $C\alpha$-atom of protein backbone and the surrounding environment pseudoatoms presented by OXY (O_2), NIC (NiEDDA) or PROT (amino-acid residue). In the calculation, four types of the spin pseudoatoms (Fig. 7 and Supplementary Fig. 6) have first been assigned to individual SL-residue of CorA before the PaDSAR calculation. The assignment was on the basis of residue-based surface exposure from an analysis of ΠO_2, $\Pi NiEDDA$ and ΔH_0^{-1} profiles. An initial configuration of modelling structure comprising the starting structure of the CorA pentamer attached with the 83 assigned spin pseudoatoms and several hundreds of OXY and NIC pseudoatoms is illustrated in Fig. 7a. The modelling of the CorA open structure may be divided into two main PaDSAR runs. The first run is carried out using the delta distance (Δr_{CB}) and accessibility restraints imposed on the starting structure as described in previous section. The protein was modelled with the united-atom CHARMM PARAM19 force field[37]. During the calculation, we restrained the N-terminal domain (residues 6–156) and secondary structures including residues 165–199, 204–237, 243–310 (stalk and TM1 helices) and 327–347 (TM2 helix). OXY and NIC pseudoatoms move within a defined boundary using the miscellaneous mean field potential in CHARMM[38]. OXY pseudoatoms were allowed to move in the

membrane region, whereas NIC pseudoatoms were distributed outside the membrane but within the defined boundary (Supplementary Fig. 6). We varied the upper and lower bound of distance restraints ($\delta = 1$ and 2) and increased MD refining cycles to generate a set of model candidates. However, it appears that these model candidates tend to lose their five-fold symmetry. Therefore, we took an individual subunit of all the resulting models and replicated their own pentamer structure. As a result, hundreds of model candidates were generated, and subsequently evaluated by considering with the following experimental-based validation: (1) the restraint penalty (P_{rstrnt}) and distance restraint violation ($viol$)[39], and (2) a consensus change between the evaluated model and the intersubunit proximity (Ω). For the former validation, P_{rstrnt} is given as

$$P_{rstrnt} = \sum k_{rstrnt} viol^2$$
$$= \sum \begin{cases} k_{rstrnt}(\Delta r_{calc} - \Delta r_{rstrnt}^{upl})^2 & \Delta r_{calc} > \Delta r_{rstrnt}^{upl} \\ 0 & \Delta r_{rstrnt}^{upl} \leq \Delta r_{calc} \leq \Delta r_{rstrnt}^{lol} \\ k_{rstrnt}(\Delta r_{calc} - \Delta r_{rstrnt}^{upl})^2 & \Delta r_{calc} < \Delta r_{rstrnt}^{lol} \end{cases} \qquad (2)$$

$$\Delta r_{calc} = \Delta r_{c\beta,i} = \Delta r_{c\beta,i,open} - \Delta r_{c\beta,i,closed} \qquad (3)$$

where Δr_{rstrnt}^{upl} and Δr_{rstrnt}^{lol} are the upper and lower distance restraints, and k_{rstrnt} is an arbitrary constant value. The latter validation was made by identifying the closer or further $C\beta$–$C\beta$ distance of individual SL residues (the short distance or first adjacent subunit) with respect to the closed-state conformation and comparing with the positive or negative signs of Ω parameters (Fig. 5). The best-fit 25 models selected based on an averaged fit criterion were subjected to structure refinement of the PaDSAR run. In the second run, the top 25 models were refined using the accessibility restraint only. Similar protocol of PaDSAR refinement described above, except no distance restraint was imposed at this step. In addition, PaDSAR treated each model as a single subunit, and refined it using the image facility within the CHARMM programme to maintain the five-fold symmetry of the CorA pentamer. In addition to the model validation described previously, inspections of the resulting structures obtained in the second run include structure convergence (RMSD), the HOLE plot[40], the accessibility mapped molecular surface and all-atom MD simulations.

Model validation by PB energy calculation of ion translocation. Model quality was assessed by calculating the solvation-free energy profile of ion translocation along the permeation pathway. We used PB continuum method to compute free-energy barrier for Mg^{2+} translocation through the CorA tranmembrane pore of the closed and open conformations. The PB calculation was performed using Adaptive PB Solver (APBS)[41]. The programme PDB2PQR was used to add hydrogen atoms and assign atomic charges and radii to each generated configuration[42,43]. Partial atomic charges and radii of the protein were taken from the CHARMM parameter sets[44]. The CorA protein was oriented with its symmetry axis coinciding with the z axis. The sequential focusing multigrid algorithm in solving PB equation consists of the following three resolution maps: $300 \times 300 \times 300$ Å^3 for coarse, $200 \times 200 \times 200$ Å^3 for medium and $100 \times 100 \times 100$ Å^3 for fine resolutions. Grid points of $161 \times 161 \times 161$ were used to all maps. The implicit membrane hydrophobic slab was defined between $z = \pm 12$ Å. This corresponds to the thickness of hydrophobic slab of 24 Å. The dielectric constants for protein, membrane and water were 2, 2 and 80, respectively[45]. Ionic strength was 0.15 M with coulomb charge $+1$ and -1, and radius 2.0 Å. Water probe radius was 1.4 Å.

The solvation-free energy profile of Mg^{2+} translocation through the TmCorA pore was computed by systematically varying Mg^{2+} positions from $z = +20$ Å (periplasmic region) to $z = -40$ Å (cytoplasmic region) with 1 Å steps along the z axis. The program APBSmem was used to set up and to monitor the membrane region[46]. For each configuration, electrostatic contribution to the solvation-free energy was computed twice, one for implicit aqueous model and one for water-membrane model, giving rise to $\Delta G_{elec,water}$ and $\Delta G_{elec,membrane}$, respectively. The solvation-free energy ($\Delta\Delta G_{elec}$) that is the electrostatic free-energy difference of the proteins embedded in the two solvent environments was obtained according to Equation (4)

$$\Delta\Delta G_{elec} = \Delta G_{elec,membrane} - \Delta G_{elec,water}. \qquad (4)$$

Model validation by explicit solvent MDs simulation. An obtained model was subsequently inserted into a pre-equilibrated lipid bilayer, made up of ~480 molecules of POPC embedded in ~64,000 TIP3P waters. Side-chain ionization states that were expected at pH = 7 were assigned based on pK_a calculations using PROPKA[47]. Sodium and chloride counter ions were added to neutralize charges on the system using VMD's Autoionize plugin[48]. Total number of atoms in the simulation is ~300,000 atoms. The MD simulations were carried out using NAMD 2.8b2 with the all-atoms CHARMM22 and CHARMM27 force fields for protein, lipid and ion[49]. The TIP3P models were used for waters. At this stage, the pseudoatoms present in the model were removed; no pseudoatom restraints were included during the simulation with explicit solvent models. To reduce finite-size effects, periodic boundary conditions were used in MDs simulations with a periodic dimension of $144 \times 144 \times 155$ Å^3. The calculation of long-rang electrostatic interactions in periodic membrane-protein system used the particle mesh Ewald

summation via fast Fourier transform (FFT). The particle mesh Ewald grid size was set to at least one cell per Angstrom in each dimension. A distance cutoff of 12 Å was used with a switching distance set at 10 Å. The non-iterative SETTLE algorithm was used to keep waters rigid. Rigid bonds between the hydrogen and the heavy atom to which it is attached were enabled. The simulations were performed at constant pressure of 1 atm and constant temperature of 300 K. Langevin dynamics was used to keep a constant temperature of the system with Langevin damping coefficient of $1 ps^{-1}$. The pressure of the system was controlled using a Noŝe–Hoove Langevin Piston. Energy minimizations and restrained MD simulations were used to relax geometric, angle, torsional and other structural distortions restrains of the model systems. During the first restrained MD run, atoms for protein and lipid head groups were restrained to their initial positions using harmonic constraints with a force constant of $1 kcal mol^{-1} Å^{-2}$. In the subsequent run, protein atoms were restrained, leaving the rest of the system to be relaxed. Finally, all positional restraints were removed and an equilibration run was performed. MD simulations were performed for 25 ns with the time step of 2 fs. The configurations and velocities were stored every 2 ps. The programs VMD, WORDOM[50], DSSP[51] and APBS[41,46] were used for assessment of protein structure stability, RMSD and visualization.

References

1. Romani, A. Cellular magnesium homeostasis. *Arch. Biochem. Biophys.* **512**, 1–23 (2011).
2. Maguire, M. E. Magnesium transporters: properties, regulation and structure. *Front. Biosci.* **11**, 3149–3163 (2006).
3. Knoop, V., Groth-Malonek, M., Gebert, M., Eifler, K. & Weyand, K. Transport of magnesium and other divalent cations: evolution of the 2-TM-GxN proteins in the MIT superfamily. *Mol. Genet. Genomics* **274**, 205–216 (2005).
4. Nelson, D. L. & Kennedy, E. P. Magnesium transport in Escherichia coli. Inhibition by cobaltous ion. *J. Biol. Chem.* **246**, 3042–3049 (1971).
5. Maguire, M. E. The structure of CorA: a Mg(2 +)-selective channel. *Curr. Opin. Struct. Biol.* **16**, 432–438 (2006).
6. Snavely, M. D., Florer, J. B., Miller, C. G. & Maguire, M. E. Magnesium transport in Salmonella typhimurium: 28Mg^{2+} transport by the CorA, MgtA, and MgtB systems. *J. Bacteriol.* **171**, 4761–4766 (1989).
7. Snavely, M. D., Florer, J. B., Miller, C. G. & Maguire, M. E. Magnesium transport in Salmonella typhimurium: expression of cloned genes for three distinct Mg^{2+} transport systems. *J. Bacteriol.* **171**, 4752–4760 (1989).
8. Eshaghi, S. et al. Crystal structure of a divalent metal ion transporter CorA at 2.9 angstrom resolution. *Science* **313**, 354–357 (2006).
9. Lunin, V. V. et al. Crystal structure of the CorA Mg^{2+} transporter. *Nature* **440**, 833–837 (2006).
10. Payandeh, J. & Pai, E. F. A structural basis for Mg^{2+} homeostasis and the CorA translocation cycle. *EMBO J.* **25**, 3762–3773 (2006).
11. Xia, Y. et al. Co^{2+} selectivity of Thermotoga maritima CorA and its inability to regulate Mg^{2+} homeostasis present a new class of CorA proteins. *J. Biol. Chem.* **286**, 16525–16532 (2011).
12. Niegowski, D. & Eshaghi, S. The CorA family: structure and function revisited. *Cell Mol. Life Sci.* **64**, 2564–2574 (2007).
13. Dalmas, O. et al. A repulsion mechanism explains magnesium permeation and selectivity in CorA. *Proc. Natl Acad. Sci. USA* **111**, 3002–3007 (2014).
14. Pfoh, R. et al. Structural asymmetry in the magnesium channel CorA points to sequential allosteric regulation. *Proc. Natl Acad. Sci. USA* **109**, 18809–18814 (2012).
15. Nordin, N. et al. Exploring the structure and function of Thermotoga maritima CorA reveals the mechanism of gating and ion selectivity in Co^{2+}/Mg^{2+} transport. *Biochem. J.* **451**, 365–374 (2013).
16. Chakrabarti, N., Neale, C., Payandeh, J., Pai, E. F. & Pomes, R. An iris-like mechanism of pore dilation in the CorA magnesium transport system. *Biophys. J.* **98**, 784–792 (2010).
17. Dalmas, O. et al. Structural dynamics of the magnesium-bound conformation of CorA in a lipid bilayer. *Structure* **18**, 868–878 (2010).
18. Guskov, A. et al. Structural insights into the mechanisms of Mg^{2+} uptake, transport, and gating by CorA. *Proc. Natl Acad. Sci. USA* **109**, 18459–18464 (2012).
19. Froschauer, E. M., Kolisek, M., Dieterich, F., Schweigel, M. & Schweyen, R. J. Fluorescence measurements of free [Mg^{2+}] by use of mag-fura 2 in Salmonella enterica. *FEMS Microbiol. Lett.* **237**, 49–55 (2004).
20. Payandeh, J. et al. Probing structure-function relationships and gating mechanisms in the CorA Mg^{2+} transport system. *J. Biol. Chem.* **283**, 11721–11733 (2008).
21. Alatossava, T., Jutte, H., Kuhn, A. & Kellenberger, E. Manipulation of intracellular magnesium content in polymyxin B nonapeptide-sensitized Escherichia coli by ionophore A23187. *J. Bacteriol.* **162**, 413–419 (1985).
22. McHaourab, H. S., Lietzow, M. A., Hideg, K. & Hubbell, W. L. Motion of spin-labeled side chains in T4 lysozyme. Correlation with protein structure and dynamics. *Biochemistry* **35**, 7692–7704 (1996).
23. Hattori, M. et al. Mg(2 +)-dependent gating of bacterial MgtE channel underlies Mg(2 +) homeostasis. *EMBO J.* **28**, 3602–3612 (2009).
24. Hattori, M., Tanaka, Y., Fukai, S., Ishitani, R. & Nureki, O. Crystal structure of the MgtE Mg^{2+} transporter. *Nature* **448**, 1072–1075 (2007).
25. Altenbach, C., Froncisz, W., Hyde, J. S. & Hubbell, W. L. Conformation of spin-labeled melittin at membrane surfaces investigated by pulse saturation recovery and continuous wave power saturation electron paramagnetic resonance. *Biophys. J.* **56**, 1183–1191 (1989).
26. Farahbakhsh, Z. T., Altenbach, C. & Hubbell, W. L. Spin labeled cysteines as sensors for protein-lipid interaction and conformation in rhodopsin. *Photochem. Photobiol.* **56**, 1019–1033 (1992).
27. Perozo, E., Cortes, D. M. & Cuello, L. G. Structural rearrangements underlying K$^+$-channel activation gating. *Science* **285**, 73–78 (1999).
28. Jeschke, G. & Polyhach, Y. Distance measurements on spin-labelled biomacromolecules by pulsed electron paramagnetic resonance. *Phys. Chem. Chem. Phys.* **9**, 1895–1910 (2007).
29. Dalmas, O., Hyde, H. C., Hulse, R. E. & Perozo, E. Symmetry-constrained analysis of pulsed double electron-electron resonance (DEER) spectroscopy reveals the dynamic nature of the KcsA activation gate. *J. Am. Chem. Soc.* **134**, 16360–16369 (2012).
30. Sompornpisut, P., Roux, B. & Perozo, E. Structural refinement of membrane proteins by restrained molecular dynamics and solvent accessibility data. *Biophys. J.* **95**, 5349–5361 (2008).
31. Starace, D. M., Stefani, E. & Bezanilla, F. Voltage-dependent proton transport by the voltage sensor of the Shaker K$^+$ channel. *Neuron* **19**, 1319–1327 (1997).
32. Nagai, T. et al. A variant of yellow fluorescent protein with fast and efficient maturation for cell-biological applications. *Nat. Biotechnol.* **20**, 87–90 (2002).
33. Dascal, N. Voltage clamp recordings from Xenopus oocytes. *Curr. Protoc. Neurosci.* **Chapter 6** (Unit 6), 12 (2001).
34. Perozo, E., Papazian, D. M., Stefani, E. & Bezanilla, F. Gating currents in Shaker K$^+$ channels. Implications for activation and inactivation models. *Biophys. J.* **62**, 160–168 discussion 169–171 (1992).
35. Jeschke, G. et al. DeerAnalysis2006—a comprehensive software package for analyzing pulsed ELDOR data. *Appl. Magn. Reson.* **30**, 473–498 (2006).
36. Brooks, B. R. et al. CHARMM: the biomolecular simulation program. *J. Comput. Chem.* **30**, 1545–1614 (2009).
37. Neria, E., Fischer, S. & Karplus, M. Simulation of activation free energies in molecular systems. *J. Chem. Phys.* **105**, 1902–1921 (1996).
38. Beglov, D. & Roux, B. Finite representation of an infinite bulk system - solvent boundary potential for computer-simulations. *J. Chem. Phys.* **100**, 9050–9063 (1994).
39. Sompornpisut, P., Liu, Y. S. & Perozo, E. Calculation of rigid-body conformational changes using restraint-driven Cartesian transformations. *Biophys. J.* **81**, 2530–2546 (2001).
40. Smart, O. S., Neduvelil, J. G., Wang, X., Wallace, B. A. & Sansom, M. S. HOLE: a program for the analysis of the pore dimensions of ion channel structural models. *J. Mol. Graph.* **14**, 354-360, 376 (1996).
41. Baker, N. A., Sept, D., Joseph, S., Holst, M. J. & McCammon, J. A. Electrostatics of nanosystems: application to microtubules and the ribosome. *Proc. Natl Acad. Sci. USA* **98**, 10037–10041 (2001).
42. Dolinsky, T. J. et al. PDB2PQR: expanding and upgrading automated preparation of biomolecular structures for molecular simulations. *Nucleic Acids Res.* **35**, W522–W525 (2007).
43. Dolinsky, T. J., Nielsen, J. E., McCammon, J. A. & Baker, N. A. PDB2PQR: an automated pipeline for the setup of Poisson-Boltzmann electrostatics calculations. *Nucleic Acids Res.* **32**, W665–W667 (2004).
44. Sitkoff, D., Sharp, K. A. & Honig, B. Accurate calculation of hydration free-energies using macroscopic solvent models. *J. Phys. Chem.* **98**, 1978–1988 (1994).
45. Grabe, M., Lecar, H., Jan, Y. N. & Jan, L. Y. A quantitative assessment of models for voltage-dependent gating of ion channels. *Proc. Natl Acad. Sci. USA* **101**, 17640–17645 (2004).
46. Callenberg, K. M. et al. APBSmem: a graphical interface for electrostatic calculations at the membrane. *PLoS ONE* **5**, pii: e12722 (2010).
47. Li, H., Robertson, A. D. & Jensen, J. H. Very fast empirical prediction and rationalization of protein pKa values. *Proteins* **61**, 704–721 (2005).
48. Humphrey, W., Dalke, A. & Schulten, K. VMD: visual molecular dynamics. *J Mol Graph* **14** (33-38), 27–38 (1996).
49. Feller, S. E. & MacKerell, A. D. An improved empirical potential energy function for molecular simulations of phospholipids. *J. Phys. Chem. B* **104**, 7510–7515 (2000).
50. Seeber, M. et al. Wordom: a user-friendly program for the analysis of molecular structures, trajectories, and free energy surfaces. *J. Comput. Chem.* **32**, 1183–1194 (2011).
51. Kabsch, W. & Sander, C. Dictionary of protein secondary structure: pattern recognition of hydrogen-bonded and geometrical features. *Biopolymers* **22**, 2577–2637 (1983).

52. Joosten, R. P. *et al.* A series of PDB related databases for everyday needs. *Nucleic Acids Res* **39**, D411–D419 (2011).

Additional information

Supplementary Information accompanies this paper at http://www.nature.com/naturecommunications

Competing financial interests: The authors declare no competing financial interests.

Reprints and permission information is available online at http://npg.nature.com/reprintsandpermissions/

How to cite this article: Dalmas, O. *et al.* Molecular Mechanism of Mg^{2+}-dependent gating in CorA. *Nat. Commun.* 5:3590 doi: 10.1038/ncomms4590 (2014).